FINAL TECHNICAL REPORT
FOR
MICROELECTROMECHANICAL PHOTONIC SWITCHES
CONTRACT NO. F49620-94-C-0009

ARPA Order Number:	A564
Program Code Number:	3D10
Amount of Contract:	$1,367,570
Name of Contractor:	Texas Instruments Incorporated 13500 N. Central Expressway P.O. Box 655936, M.S. 105 Dallas, Texas 75265
Effective Date of Contract:	15 December 1993
Contract Expiration Date:	14 February 1997
Contract Number:	F49620-94-C-0009
Program Manager:	P.A. Congdon (214) 995-2056
Short Title of Work:	MEMS

11 July 1997

Sponsored by
Defense Research Projects Agency
ARPA Order No. A564
Monitored by AFOSR Under Contract No. F49620-94-C-0009

REPORT DOCUMENTATION PAGE

Form Approved
OMB No. 0704-0188

1. AGENCY USE ONLY (Leave blank)	2. REPORT DATE	3. REPORT TYPE AND DATES COVERED
		FINAL REPORT -15 Dec 93 - 14 Dec 96

4. TITLE AND SUBTITLE

Microelectromechanical Photonic Switches

5. FUNDING NUMBERS

A564/31
61101E

6. AUTHOR(S)

Dr Collins

AFOSR-TR-97

0309

7. PERFORMING ORGANIZATION NAME(S) AND ADDRESS(ES)

Texas Instruments, Inc
CTRL Research laboratories
P O Box 655936, M/S 105
Dallas, TX 75266-5936

9. SPONSORING/MONITORING AGENCY NAME(S) AND ADDRESS(ES)

AFOSR/NE
110 Duncan Avenue Suite B115
Bolling AFB DC 20332-8050

10. SPONSORING/MONITORING AGENCY REPORT NUMBER

F49620-94-C-0009

11. SUPPLEMENTARY NOTES

12a. DISTRIBUTION/AVAILABILITY STATEMENT

APPROVED FOR PUBLIC RELEASE: DISTRIBUTION UNLIMITED

12b. DISTRIBUTION CODE

13. ABSTRACT *(Maximum 200 words)*

TI has successfuly fabricated asymmetrical micromirrors up to 350 um long for fiber-optic shutter applications. We overcame the challenge of maintaining straightness in mirror sizes 50 um by modifying the conventional micromirror process. There are several different options for process modeling and optimization. We chose a corrugated structure because of the simple process modification and optimum bending curvature. Modeling showed a 41-fold curvature reduction. Fabricated corrugated structures exhibited a 19.8X straightness improvement. In addition, a simple layout design modifaction to increase the tile angle provided a boost in shutter performance. We consolidated first-pass results from working asymmetrical mirrors to design and fabricate a second chip to be packaged in a miniaturized 4 X 4 fiber-optic crossbar system. A 350-um long mirror with a r-um spacer enables the mirror to block 80-um beams. We designed and fabricated a package to host the crossbar swtich points.

14. SUBJECT TERMS

15. NUMBER OF PAGES

16. PRICE CODE

17. SECURITY CLASSIFICATION OF REPORT	18. SECURITY CLASSIFICATION OF THIS PAGE	19. SECURITY CLASSIFICATION OF ABSTRACT	20. LIMITATION OF ABSTRACT
UNCLASSIFIED	UNCLASSIFIED	UNCLASSIFIED	

FINAL TECHNICAL REPORT
FOR
MICROELECTROMECHANICAL PHOTONIC SWITCHES
CONTRACT NO. F49620-C-0009

T.H. Lin, G.A. Magel, and P. Congdon
Texas Instruments Incorporated, Dallas, TX 75265

EXECUTIVE SUMMARY

TI has successfully fabricated asymmetrical micromirrors up to 350 μm long for fiber-optic shutter applications. We overcame the challenge of maintaining straightness in mirror sizes >50 μm by modifying the conventional micromirror process. There are several different options for process modeling and optimization. We chose a corrugated structure because of the simple process modification and optimum bending curvature. Modeling showed a 41-fold curvature reduction. Fabricated corrugated structures exhibited a 19.8× straightness improvemement. In addition, a simple layout design modification to increase the tilt angle provided a boost in shutter performance.

We consolidated first-pass results from working asymmetrical mirrors to design and fabricate a second chip to be packaged in a miniaturized 4 × 4 fiber-optic crossbar system. A 350-μm long mirror with a 4-μm spacer enables the mirror to block 80-μm beams. We designed and fabricated a package to host the crossbar switch points. This package includes the shutter chip, optical fiber hosting chips with V-grooves, and 1:1 image transfer microlenses. The insertion loss of this system, constructed with single-mode fiber components, is 12 dB optical, plus excess losses in the splitters, shutter switches, and fiber-optic coupling. Packaging and fixtures were designed to simplify optical alignment. Optical measurement will extract the extinction ratio, insertion loss, crosstalk, and actuation speed, all in an alignment fixture. After this optimization, the package can be locked to remain in alignment after removal from the fixture, resulting in a compact 16-channel on-off switch assembly.

Final assembly and full optical characterization remain to be done.

I. INTRODUCTION

Photonics, specifically fiber optics, is already used heavily in data and voice transmission. The enormous intrinsic bandwidth of the transmission medium (>10 THz) is just beginning to be tapped. Currently, all data and voice switching are done electronically; that is, optical signals must be converted into electrical ones for switching and then converted back to optical signals for retransmission. This is an inefficient and costly process, and the interposed electronic circuitry limits the data rates that can pass through it. Photonic switches that perform signal switching while remaining in the optical domain will be critical components for future high-performance data, voice, and image transmission and processing systems.

Relatively expensive, ultra-high-speed electro-optic switches for time-slot interchangers at central switching locations will be needed, as well as a large volume of low-cost, intermediate-speed switches located closer to the individual users. Micromechanical optical devices fill this latter gap in the speed/cost hierarchy, which remains unaddressed by other switching technologies. Micromechanical switches also promise much higher extinction ratios than are achievable using electro-optic devices.

Many of the classical switching network architectures found in electronics and communications could be implemented with photonic switching elements to synthesize photonic switching networks.[1,2] Switching network architectures include the crossbar, Clos, Benes, Banyan, Omega, and shuffle networks, among others. These architectures vary in properties such as crosstalk, attenuation, number of switches traversed, and number of signal line crossovers. Networks that are "nonblocking" allow any input-to-output connection to be made without preventing other input-to-output connections from being made simultaneously. Networks with "broadcast" capability allow one input to be connected to multiple outputs simultaneously. "Full broadcast capability" refers to the property that any input can be simultaneously connected to *all* outputs. In the classical crossbar implementation, each input is fanned out to all the outputs, and at each output, the lines from all the inputs are fanned in. The crossbar architecture often is used as a baseline for comparison because (1) only one signal is routed through each switch point, thus minimizing the effect of switch crosstalk,

and (2) maximum *connectivity* is achieved (i.e., the maximum number of connections between the inputs and outputs are obtained). Information gathered in implementing a crossbar network using a particular type of switching element is readily applied to predict the performance of other switching architectures formed from the same switching element.

This report discusses the design and fabrication of micromachined optical components and packages that will leverage highly developed integrated circuit fabrication technology and inexpensive silicon-compatible materials to produce low-cost, rugged, small, lightweight, high-performance optical switches for a variety of military and commercial applications and environments. Micromachining plays multiple roles in producing these switches: surface micromachining of aluminum forms the optical shutters or mirrors that perform the switching, and bulk micromachining of silicon forms prealigned fiber holders.

Torsional micromirror devices [3,4] operate as binary amplitude modulators by deflecting light into and out of the optical system. TI has launched a product series using torsional digital micromirror devices for projection display and hard copy applications. Figure 1 illustrates the structure of a simple torsional micromirror device. When a potential difference is applied between an address electrode and a pixel, the electrostatic attraction causes the pixel to rotate about its hinge axis. On full rotation, the pixel is in contact with a landing electrode, which is held at the same potential as the pixel. This prevents shorting of the pixel with the silicon substrate. Note that Figure 1 shows two landing and address electrodes, which allow the pixel to be rotated in either direction. The mirror size and the spacer thickness are typically designed so that each landing is at a 10-degree tilt from the flat position.

In previous work[5], TI demonstrated a 4×4 multimode fiber crossbar switch based on the reflection of light from the bistable mirror element shown in Figure 2 that connects two fibers optically. Figure 3 shows the principle of operation for this switch point. A microlens optical system forms a one-to-one image of the input fiber core on the 50-μm diameter micromirror. The mirror is tilted to one landing position, and a similar optical system forms a one-to-one image of the light reflected off the micromirror into the receive fiber. To turn the switch off, the micromirror is

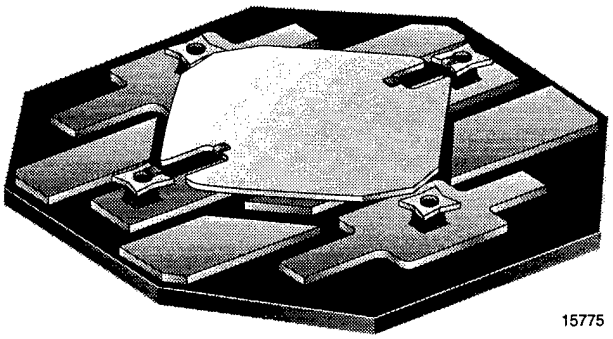

Figure 1. Landing and address electrodes of a torsional micromirror.

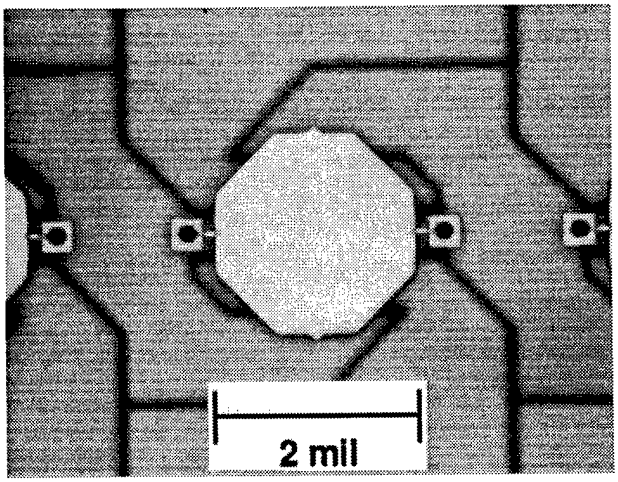

Figure 2. Torsional micromirror used for first TI 4 × 4 crossbar switch.

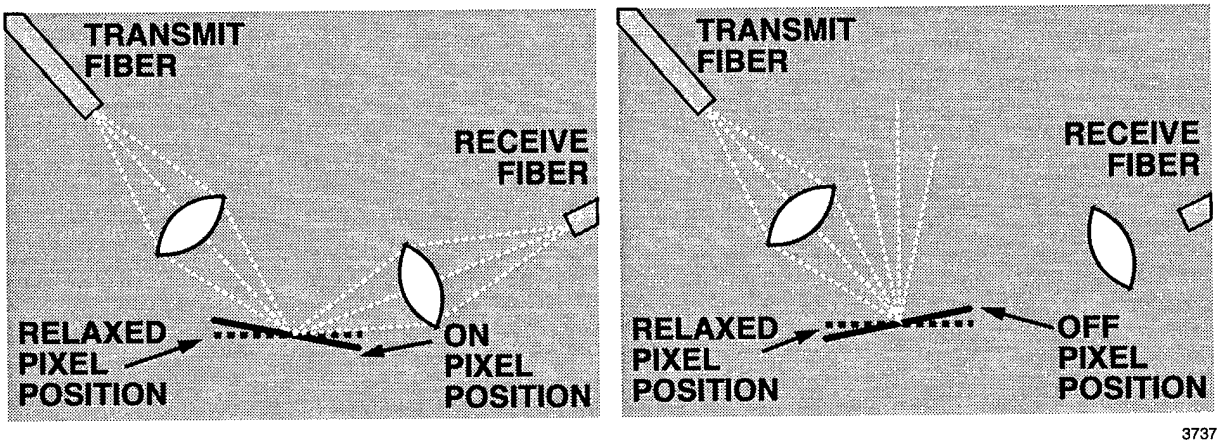

Figure 3. On and off states of the micromirror-based fiber-optic switch.

tilted to the opposite extreme and the light is deflected from the aperture of the output lens so that no light reaches the output fiber. Figure 4 is a schematic diagram of this 4 × 4 crossbar switch. Maximum contrast ratio is obtained when the angular tilt of the micromirror exceeds the numerical aperture of the optical system. Contrast ratios of 72.9 dB (19.68×10^6:1) have been obtained in a single-point switch using single-mode fiber, and 43 dB (20,000:1) in a single-point switch using a 50-μm core multimode fiber. To synthesize a 4 × 4 crossbar, 16 on/off switch elements were interconnected with 1 × 4 splitters and 4 × 1 combiners. The same approach is used in our configuration. An insertion loss of 18.7 dB, extinction ratio of 27.3 dB, and crosstalk level of –28.5 dB were achieved in this early demonstration.

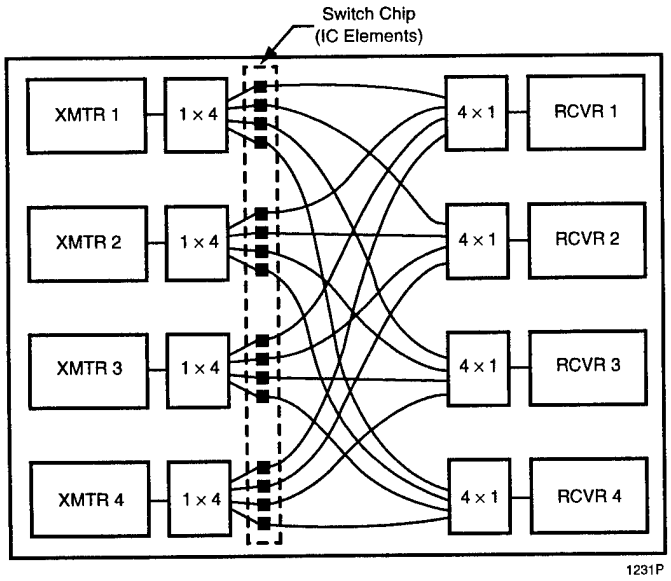

Figure 4. Schematic diagram of a 4 × 4 crossbar switch.

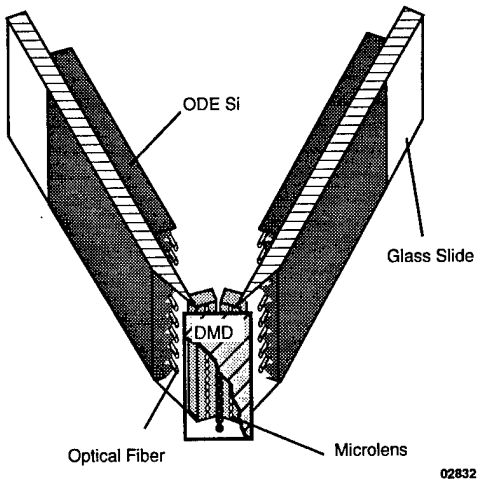

Figure 5. Demonstrated 4 × 4 cross-bar switch on optical table.

Although the results obtained in the earlier demonstration were promising, we instituted a number of improvements to simplify optical assembly for this program. The physical arrangement of the optical elements in the previous switch is illustrated in Figure 5. Although aided by the use of microlens arrays and silicon V-groove fiber holders, this arrangement required tedious manual alignment and could not be integrated into a flat-profile package. This was because input and output fibers/lens arrays had to be aimed at an angle to the micromirror that matched its tilt angle. To address the packaging and insertion loss concerns, we developed a monolithic in-line on/off switch that relies on the shutter action of a new asymmetric micromirror element to block the light in the off state. An in-line monolithic and/or self-aligned flat package in which the fibers could remain coplanar would result in a more compact and rugged package. We can reduce insertion loss by avoiding the use of a reflection from the micromirror in the on state. Instead, we couple the input and output fibers using an in-line arrangement in which the optical beam passes over the chip undisturbed in the on state. The micromirror thus need not be of optical quality, since it acts only as a shutter.

Figure 6 shows the concept drawing of this switch. A microlens forms a 1:1 image of the light from an optical fiber at the position of an asymmetric torsion mirror element. When the switch is on, the mirror is unaddressed and flat and the light is re-imaged through another microlens onto

Figure 6. Conceptual drawing of shutter-based in-line fiber-optic crossbar switch system.

the output fiber. When the switch is off, the actuator arm of the micromirror element is addressed and the shutter arm rises into the space between the microlenses. This interrupts the optical path and scatters the light out of the plane of the device.

This in-line on/off switch has several advantages over the previous switch architecture. The position of the transmit and receive fibers in relation to each other and the position of the mirrors in relation to the fiber can be defined photolithographically. This eliminates tedious mechanical alignment and lowers the insertion loss. The in-line on/off switch is designed with a large shutter to block all the light in the optical path, giving a high extinction ratio and low crosstalk.

II. CALCULATION OF SHUTTER GEOMETRY

Figure 7 shows that the angle of rotation is determined by the length, l, of the actuator arm and the height of the mirror above the substrate as determined by the spacer thickness d: $\sin\theta = d/l$. The height, h, that the shutter arm length rises above its flat or undeflected state is then $h = L\sin\theta = Ld/l$.

These equations can be used to calculate the required shutter pixel dimensions. First, at least 99% of total power should be blocked. Second, the diameter of the optical beam to be blocked at the ends of the Rayleigh range (z_R) is $H_{min} = \sqrt{2^D}$, where D is the diameter of the 99% power point at the beam waist (Figure 8). Third, the maximum total length for the long end and the short end of the torsional mirror should not exceed $2z_R$ so that it allows the optical beam to pass without clipping in the on state. Table 1 lists the size of H_{min} and z_R for single-mode fiber and multimode fiber.

To block the light from the 1:1 image of a 50-μm core multimode fiber, H must be at least 50 μm—preferably more, perhaps 100 μm. A 10-μm core single-mode fiber would require $H \approx 20$ μm. Figure 9 is a plot of the shutter length L required for single- and multiple-mode fiber as a function

Table 1. Beam diameters to be blocked in the switching system

	H_{min} (μm)	z_R (μm)
Single Mode	20	52
Multimode Equivalent	100	260

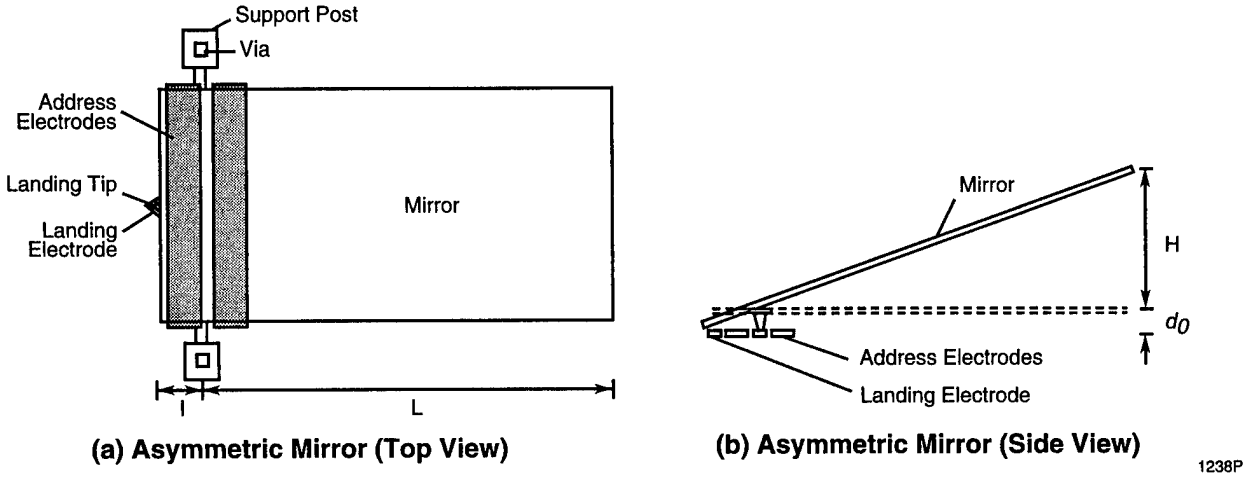

Figure 7. In-line fiber-optic switch using asymmetric tilting mirror element as an on/off shutter.

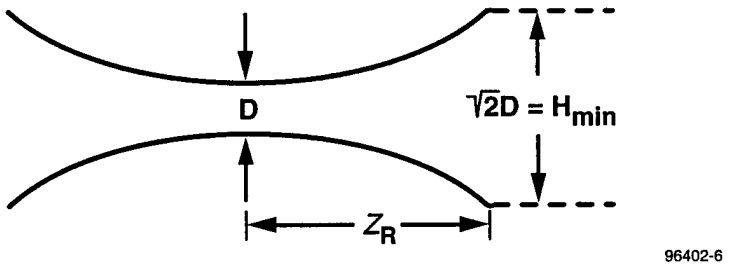

Figure 8. The minimum value of H_{min} obtained by computing Rayleigh range and Gaussian beam size at 99% power point.

of tilt angle θ. Current micromirror designs use a deflection angle of around 10 degrees. A multimode switch with a tilt angle of 10 degrees would require a shutter arm nearly 600 μm long, whereas a single-mode switch requires a 100-μm shutter arm. The largest torsion elements we fabricated previously were a little over 100 μm in diameter. Thus, we should be able to use micromirror fabrication techniques to build at least a single-mode switch.

Furthermore, the single-mode H_{min} shown in Table 1 is calculated under the assumption that the fibers can be placed right against both sides of the mirror. In reality, the fibers are at some

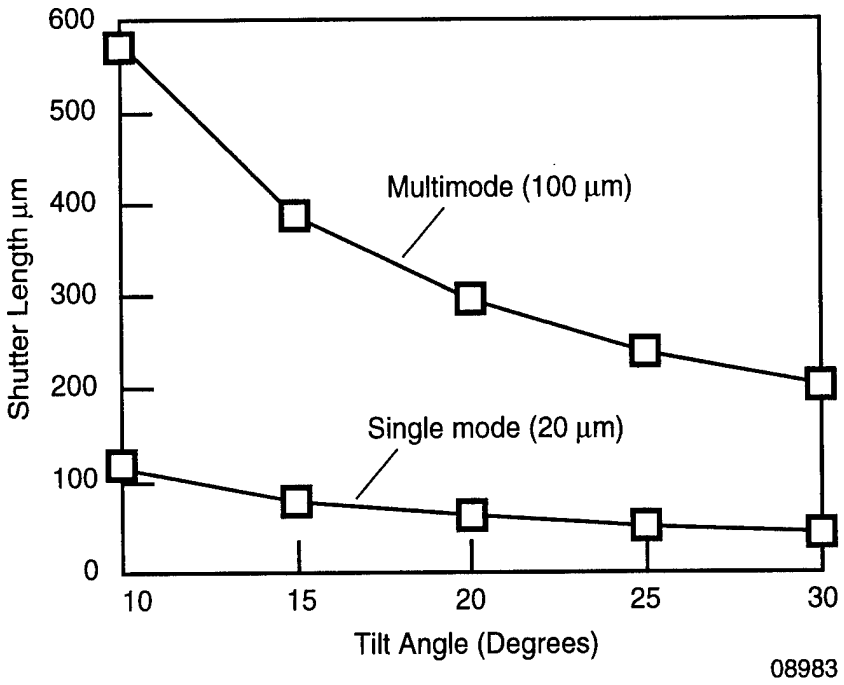

Figure 9. Required shutter length versus tilt angle for single-mode and multimode in-line fiber switch based on asymmetric micromirror.

small distance from the mirror because of handling and packaging concerns. In other words, H_{min} will be larger than the number in Table 1. Therefore, we must build as large a mirror as process and structure allow.

We know from experience that film stresses and stress gradients do exist and that larger mirrors are more likely to distort. For a smaller mirror size, we need a larger tilt angle to block the beam. However, hinge torsion at a large angle will cause severe hinge stresses. To determine a reasonable size for fabrication and a reasonable angle to twist the hinge, we designed a torsion-hinge test structure that covers pixel lengths from 13 to 27 µm on the short arm and 75 to 350 µm on the long end, with pixel widths of 30 and 80 µm, and with several hinge geometries. Figure 10 shows the layout of the torsion hinge test structure chip that covers various long-arm and short-end lengths and widths of the micromirror.

Figure 11 shows the relationship between short-end length and spacer thickness and tilt angles. Figure 11 indicates, for example, that we need a 15-µm spacer for the 30-µm short arm to land at 30 degrees.

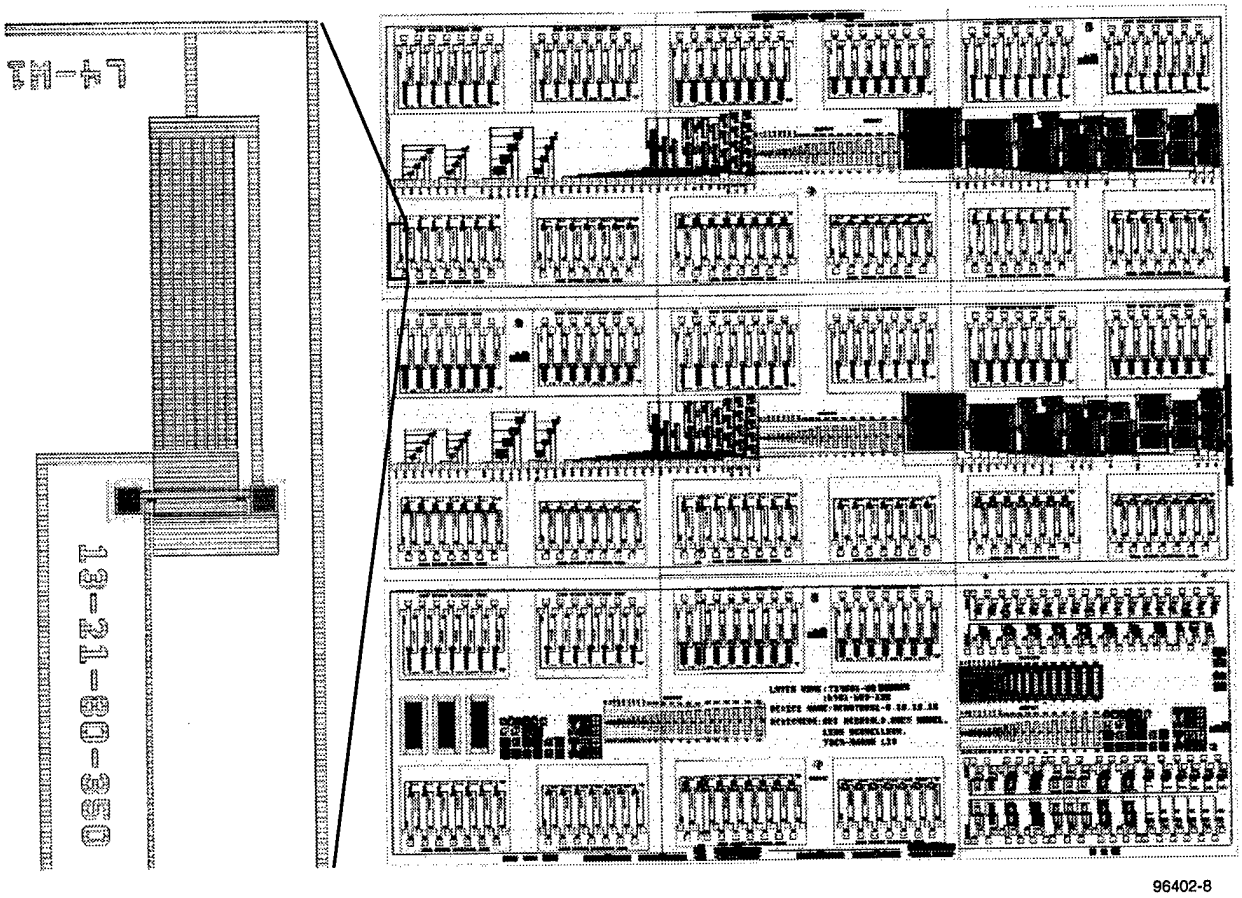

Figure 10. Layout of torsion hinge test structure chip that covers various long-arm and short-arm lengths and widths of the micromirror.

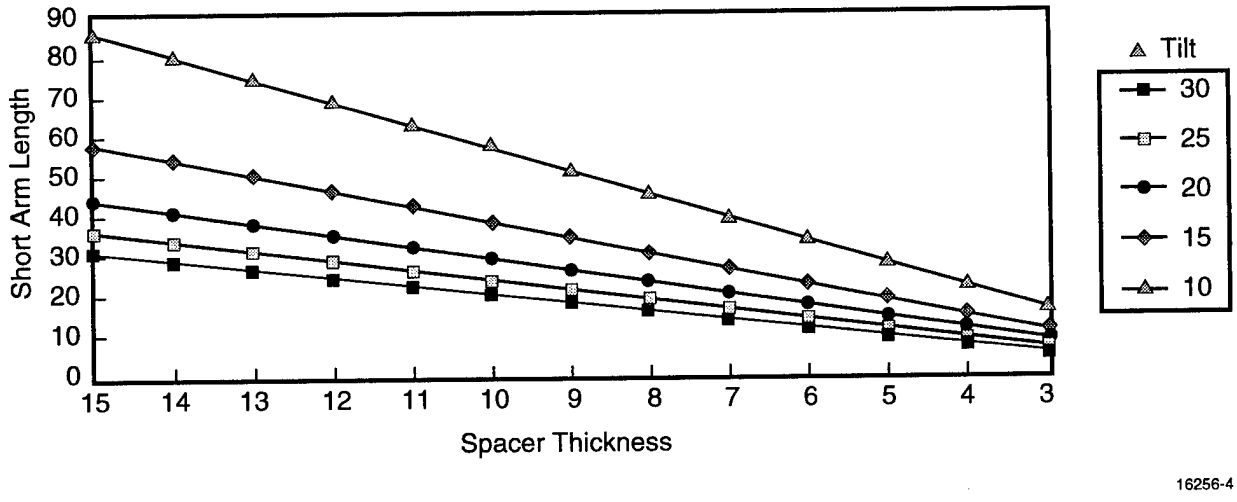

Figure 11. Relationship between short-end lengths, spacer thickness, and angles.

III. CONVENTIONAL MICROMIRROR PROCESS AND ISSUES

The conventional micromirror process includes four layers: (1) electrode, (2) spacer, (3) hinge, and (4) mirror. Recently, TI developed the hidden-hinge process[6] for projection display applications. This process uses an additional mirror layer to shield the nonactive optical areas such as post and hinge. We use a conventional process to reduce process time and cost and, eventually, to obtain a better yield. Our first process used normal 2-μm spacers and normal process flow, described as follows.

The micromirror process[3] is completely independent of the process for the underlying address circuit. It consists of four layers called the micromirror superstructure (electrode, spacer, hinge, beam). The superstructure process (Figure 12) begins with a completed address circuit including electrode contact openings formed in the protective oxide of the address circuit. An aluminum alloy that forms the address electrode [Figure 12 (a)] is sputter-deposited onto the protective oxide, making contact with the underlying address circuit through openings in the protective oxide. The electrode is patterned with a plasma etch. A planarizing organic spacer (typically 2 to 3 μm thick) is then spun over the electrode and patterned with openings that will form the support posts.

The remaining two layers are then formed by the so-called buried-hinge process [Figure 12(b)]. An aluminum alloy that forms the hinge (typically 500 to 1000 Å thick) is sputter-deposited onto the spacer. A masking oxide is plasma-deposited and patterned outside the areas that are to form the hinges. This hinge oxide is then buried by a second aluminum alloy layer that is to form the beam (typically 3000 to 5000 Å thick). Next, a masking oxide is plasma-deposited and patterned outside the areas that are to form the beams and support posts.

Finally, a single plasma aluminum etch forms the pattern on the hinges, beams, and support posts. The beam metal overlying the hinge region is etched away, exposing the buried-hinge oxide, which acts as an etch stop. When the plasma aluminum etch is complete, regions of thin hinge metal and thick beam and support-post metal have been simultaneously patterned.

This completes the micromirror superstructure process at the wafer level. The masking oxide for the hinges, beams, and support posts is left in place. The wafers are then sawed into

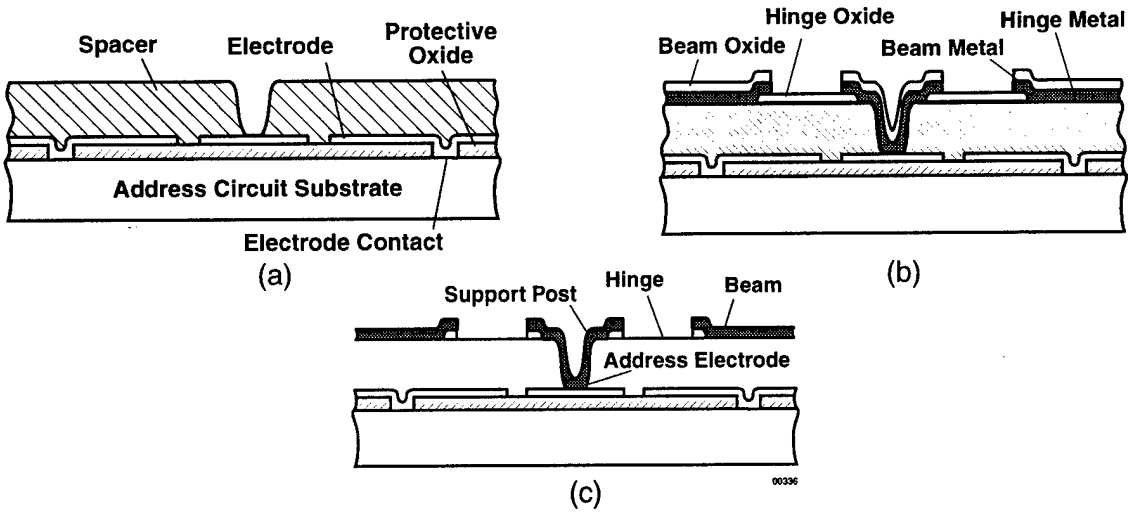

Figure 12. Steps in micromirror fabrication.

individual chips. Finally, the chips are placed in a plasma etching chamber, where the masking oxide is removed and the spacer is isotropically etched from under the beams to form the air gaps [Figure 12(c)]. Plasma undercutting of the beams after the wafer has been sawed into individual chips eliminates all possibility of hinge breakage and chemical contamination.

The final structure of the mirror should look like Figure 13. Two issues are associated with this process: (1) a 2-μm spacer will provide only 10 degrees of tilt angle with l = 17 μm, as shown in Figure 11, which may be insufficient for shutter applications; (2) plasma deposition of aluminum alloy always leaves stresses in the film. The stresses cause the mirror to curl. Figure 14 is a SEM photograph of a 350-μm long mirror fabricated using the conventional process. The mirror curled more than 10 μm in the middle and both sides landed at the tips. Figure 15 is an interferometric picture of the same device. The number of fringes are measured to be 10 μm from the middle to the tip. If the hinges did not hold it down, the curvature could be even more severe. A mirror of this size would be useless without a reinforcement structure to make it straight. In addition, any thermal cycle can change the stress, causing more curling. We also discovered that these devices are subject to excessive heat from plasma undercut if there are no etching access holes.

IV. OPTIONS TO MODIFY PROCESS AND STRUCTURE

We have limited options to build in the reinforcement structure because the micromirror process is a microfabrication surface-micromachining process. The first option is a bilayer struc-

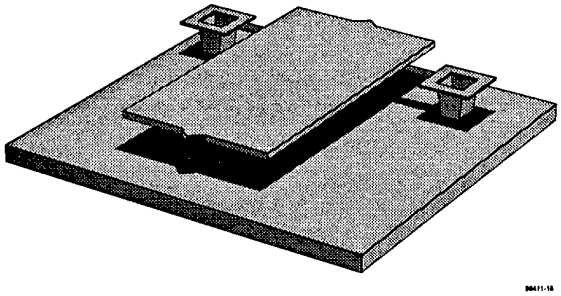

Figure 13. Perspective view of asymmetrical micromirror from conventional mirror process.

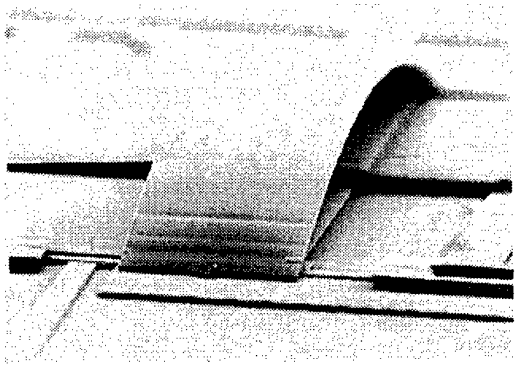

96402-7

Figure 14. SEM photograph of 350 μm long mirror fabricated using conventional process.

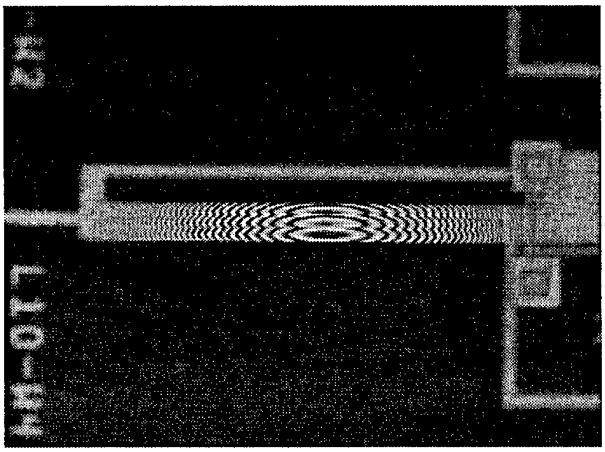

96402-9

Figure 15. Interferometric picture of device shown in Figure 14.

ture using the newly developed standard hidden-hinge process[6]. The main difference in building a projection display device and this optical shutter device is in using the hinge layer as a corrugated layer to bind the two metal layers, just like cardboard box material (Figure 16).

Another option is to modify the conventional process by adding another spacer and to corrugate the shape of the long-arm area before we process the hinge and mirror level (Figure 17). This corrugated monolayer structure not only reduces curvature but also acts as an additional spacer thickness for a larger tilt angle.

V. STRUCTURAL MODELING AND OPTIMIZATION

The development of thin film stresses during deposition and the subsequent thermal treatment is well recognized in silicon processing. Such stresses reveal themselves in two ways: (1) a

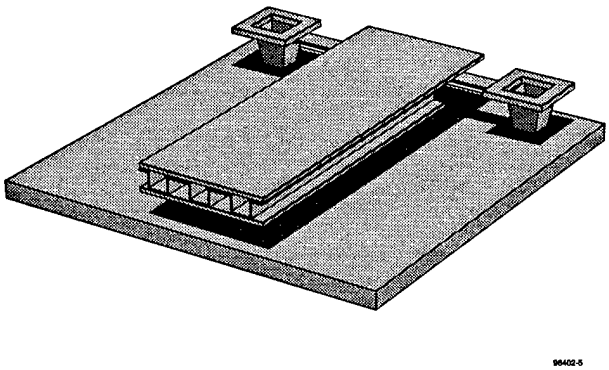

Figure 16. Bound bilayer structure.

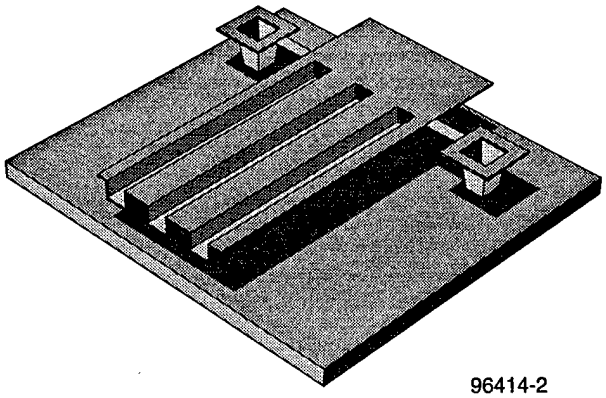

Figure 17. Perspective view of optical shutter device using a corrugated structure.

tendency of a film to change the in-plane dimensions, and (2) a tendency of a film to curl when the constraint from the substrate is removed. We will call the first kind the "film stress" and the second kind the "stress gradient" in the following discussion. While it may be desirable to minimize the film stress and the stress gradient via optimization, the complexity and the inherent process variability of plasma deposition make it impractical. Instead, our strategy is to optimize the design so that the impact of such stresses and stress gradients on the final mirror curvature is minimized.

The deflection of a planar structure is well described by the classical beam and plate theories of Timoshenko[7,8]. The out-of-plane curvature is proportional to M/I, where M is the bending moment the structure is subjected to and I is the cross-sectional moment of inertia. In the case of a free-standing structure, M can be thought of as the bending moment needed to straighten the planar structure.

Film stress by itself does not result in a curling mirror as in Figure 14. The difference in the film stresses in a multiple-film stack, however, can be a significant factor causing curvature of the overall structure.

Note that the contiguous aluminum hinge and mirror layers in Figure 12 can have very different stresses because of their very different thicknesses and thermal histories. The observed mirror curvature in Figure 14 is probably caused by a combination of the film stress difference between the two aluminum layers and the stress gradient within each individual layer.

It is natural to increase the cross-sectional moment of inertia in an attempt to reduce the

mirror curvature. This goal can be achieved with either the bound bilayer or the corrugated monolayer. Such cross-sectional modifications do not change the bending moment originating from the stress gradients in the individual layers. The bending moment caused by the film stress difference between different layers, however, can increase with the cross-sectional moment of inertia. The ratio between the latter bending moment to the cross-sectional moment of inertia is, therefore, useful as a figure of merit. We analyzed the two options mentioned in Section IV and optimized the monolayer design for implementation. Only bending in the length direction is considered here for simplicity. In addition, the maximum allowable corrugated depth is 2 μm.

Bound Bilayer Structure

A thin, corrugated hinge layer can be used to bind the two mirror layers in this structure, shown in Figures 16 and 18. Let t_1, t_2, and t_3 denote the thicknesses of the bottom, top, and hinge layers, respectively.

We anticipate $t_1 \sim t_2 >> t_3$ using the fabrication technique described in Section III. When the spacer thickness, *d*, is sufficiently greater than the two outer aluminum layers, the cross-sectional moment of inertia is dominated by the two outer layers. Only the two parallel outer layers of thickness, t_1 and t_2, need to be considered for the purpose of modeling. The moment of inertia per unit mirror width, *I*, of the bilayer cross section is simply

$$I = \frac{t_1^3 + t_2^3}{12} + \frac{(2d' + t_1 + t_2)^2 t_1 t_2}{4(t_1 + t_2)} \tag{1}$$

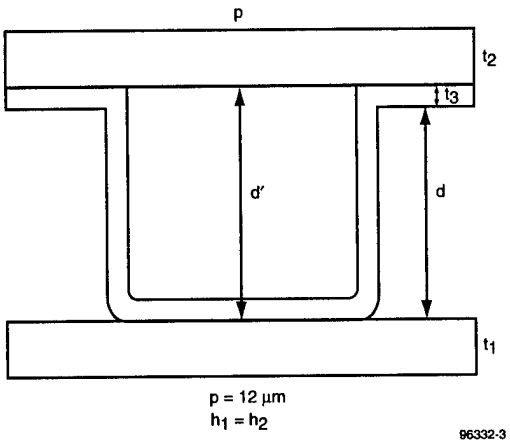

Figure 18. Actual cross section of a bound bilayer structure.

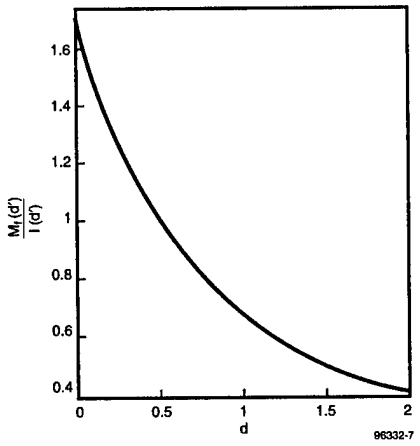

Figure 19. Curvature versus separation between the two bound layers.

where $d' = d + t_3$ is the separation between the two outer layers. The bending moment caused by the film stress difference is calculated in the following manner. Let σ_2 and σ_1 be the film stresses of the top and the bottom layers, respectively, before they are released from the substrate. The film stress difference $(\Delta\sigma)$ between the two layers is defined as $\Delta\sigma = \sigma_2 - \sigma_1$.

In the absence of stress gradients, the bilayer can be kept flat if an additional stress $\Delta\sigma$ is placed in the bottom layer. This is equivalent to a bending moment M_f per unit mirror width, given by

$$M_f = t_1 \cdot d_1' \cdot \Delta\sigma = \frac{1}{2}\left(\frac{t_2 + t_1}{t_2 + t_1}\right)(2d' + t_2 + t_1)\Delta\sigma \qquad (2)$$

where d_1' is the distance between the center of the bottom layer and the neutral surface of the bilayer cross section. When the substrate constraint is etched away, the bending of the bilayer is equivalent to that caused by a bending moment of $-M_f$. Note that, while $I \propto d'^2$ for large values of d', $M_f \propto d'$ at the same time.

Figure 19 shows how the film separation (d') affects the figure of merit, M_f/I, when t_1 = 4350 Å and t_2 = 3700 Å are given from an existing process flow. A 4.1× curvature reduction is achieved when d' reaches 2 μm.

Corrugated Monolayer Structure

It is also possible to construct a cross section as in Figure 20. Assuming 100% step coverage, we can calculate I and M_f as:

$$I = \frac{1}{12(p+2d)}\left\{p(p+8d)(t_2+t_1)^3 + 12pd^2(2r-1)(t_2+t_1)\left[d^2 + 2dp + 3rp^2(1-r)\right]\right\} \qquad (3)$$

$$M_f = \left(\frac{t_2 t_1}{2}\right)\left(1 + \frac{4d}{p}\right)\Delta\sigma \qquad (4)$$

where $r = (s/p)$ is called the corrugation duty cycle.

We expect again that $I \propto d^2$ for d much greater than t_2 and t_1 and p sufficiently large. Obviously, the maximum allowable value for d is preferred. The bending moment M_f, curiously, is less than linearly dependent on d. For p >> d, M_f is nearly stationary. This results because the hinge film is on both sides of the neutral surface, which leads to considerable bending-moment cancellation. Figure 21 shows how the reduction of (M_f/I) varies with the corrugation duty cycle and the

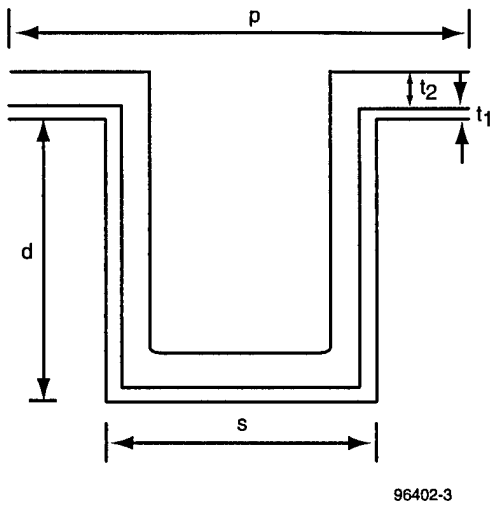

Figure 20. Cross section of a corrugated monolayer. The pattern can repeat many times with a pitch p.

pitch p when t_2 = 3700 Å, t_1 = 600 Å, and d = 2 μm. Greater than 50-fold curvature reduction can be achieved with p = 20 μm and a duty cycle slightly higher than 0.5. However, we chose p = 10 μm to prevent overheating in the plasma undercutting process.

Our earlier result in Figure 14 is basically a monolayer when d = 0, and d = 2 corresponds to our new design. Using a convenient 50% duty cycle, p = 10 μm and d = 2 μm, 41× improvement in curvature reduction can be achieved, as shown in Figure 22.

VI. RESULTS AND DISCUSSION

Micromirror Straightness Through Reinforcement

The 350-μm long arm curls up severely after releasing the spacer because of the stress in the metal film (Figure 14). In the new process, we implemented the corrugated structure, and we added periodic access holes to reduce plasma undercut time. Figure 23 shows that our mirror maintains straightness with the same stress conditions as in the metal film. Figure 24 is an interferometric photograph of the same device in a non-tilting state, showing only 0.5-μm variation from the middle of the 350-μm long arm to the tip.

We can calculate the radius of curvature by using simple geometry and approximations as shown in Figure 25.

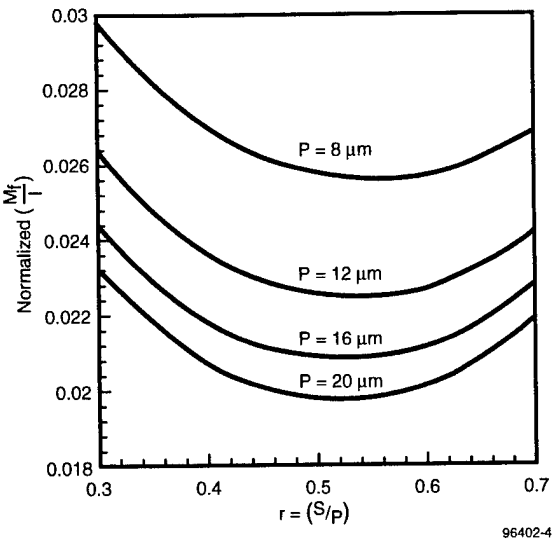

Figure 21. $\left.\frac{M_f}{I}\right|_{d=2\mu m}$ **normalized against** $\left.\frac{M_f}{I}\right|_{d=0}$

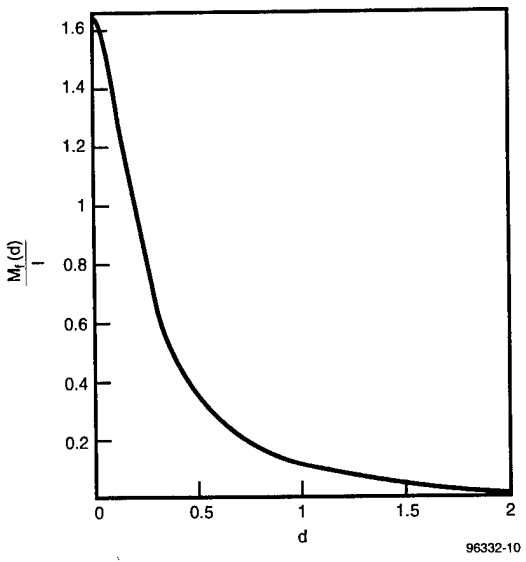

Figure 22. Inverse radius of curvature versus depth of the ditch.

$$\frac{2b}{a}=\frac{a}{R}$$

$$R=\frac{a^2}{2b}$$

if R > > a

$$2a \approx 2R\theta = 350\ \mu m$$

For the noncorrugated structure:

b = 10 µm

R = 1.53 mm

For the corrugated structure:

b = 0.5 µm

R = 30.3 mm

With the corrugated structure, we obtained a 19.8× improvement in radius of curvature over that of the noncorrugated structure.

The improvement of the radius of curvature by a factor of 41 predicted by the theory in Section V is difficult to verify because the radius of curvature in the noncorrugated structure should be larger than that in the photograph in Figure 14 while restrained by the hinge. Meanwhile, the heating effect of plasma is significantly reduced by the short undercut times that result from using

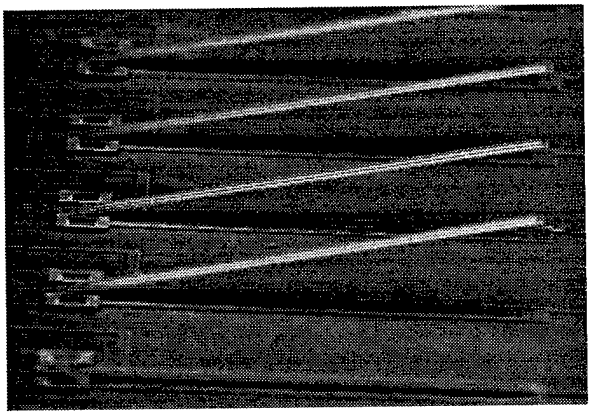

96402-10

Figure 23. SEM photograph of a 35-μm long × 30-μm wide micromirror in actuated position.

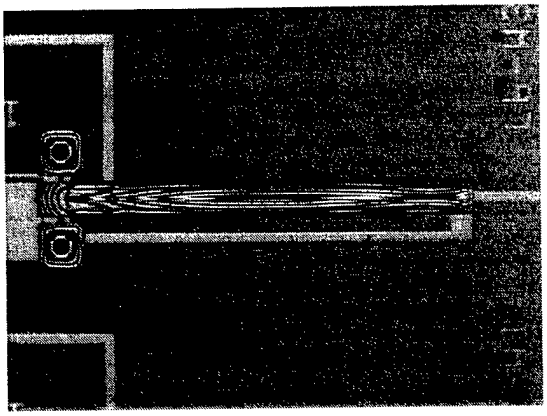

96402-11

Figure 24. Interferometric photo of the device in Figure 23 in a nontilting state.

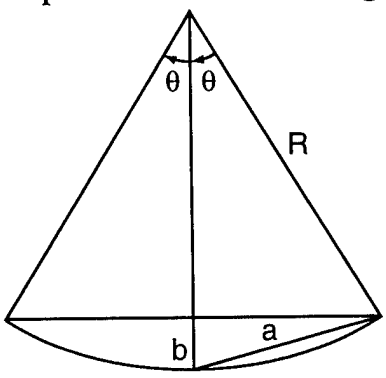

Figure 25. Geometrical representation of mirror curling.

access holes in the corrugated structure. The end result of the radius of curvature is that it is significantly improved by the corrugated structure and shorter plasma time.

Micromirror Functional Test

The first successful batch of long mirrors was put under test. The basic functional test was in the cleanroom to observe movement. Figure 26 shows the test setup based on a probe station. Mirror movement is controlled by a 1 Hz variable voltage square wave signal. The onset voltage changes, depending on the electrode size. So far, there are not enough data to show the voltage-versus-size relationship. However, we demonstrated the feasibility of the 350-μm mirror. We then calculated the need for a 350-μm long mirror to rise 80 μm in the optical system to block the beam under packaging constraints. Figure 27 shows the 350-μm long mirror in the up and down positions. We further characterized the speed of this device; Figure 28 illustrates the speed measurement facility. Figure 29 shows the typical speed of the 350-μm long mirror, indicating 500-μs rise and fall times.

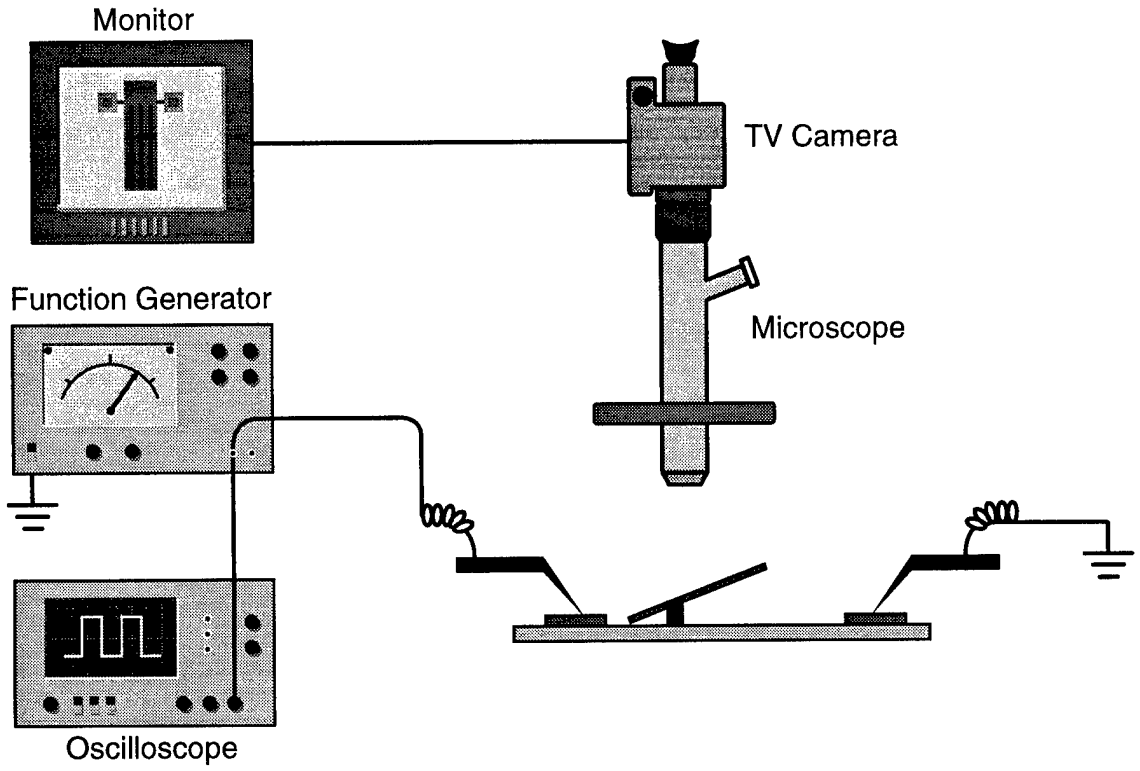

Figure 26. Functional test setup at cleanroom; 350-μm long, 30-μm wide mirror captured in motion from video in (a) up position and (b) down position.

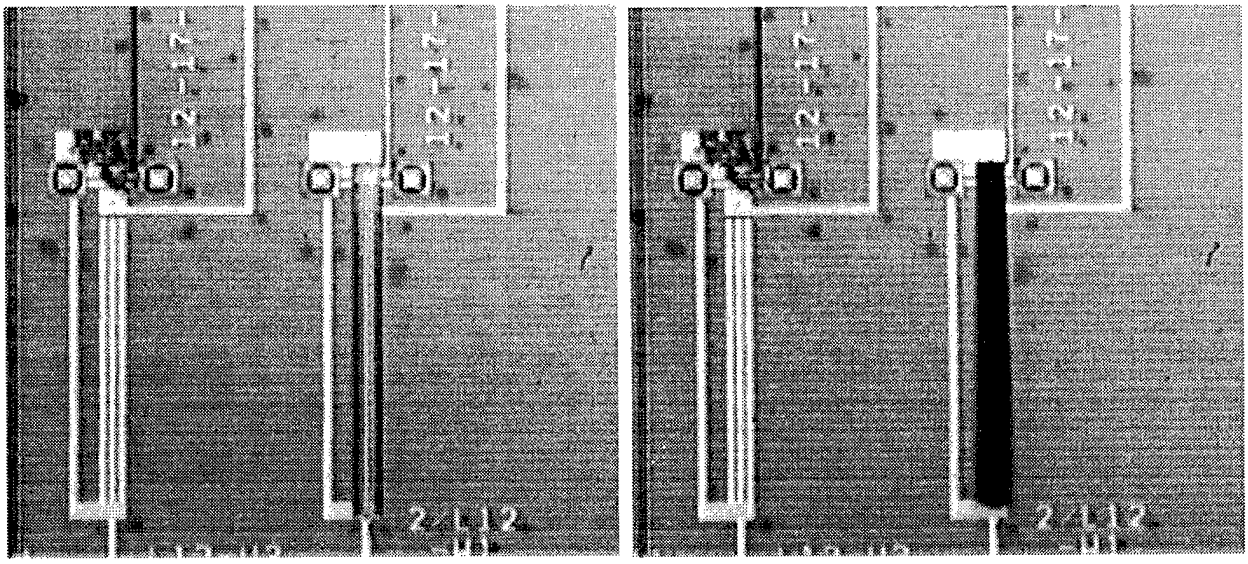

(a) (b)

Figure 27. Micromirror photonic switches.

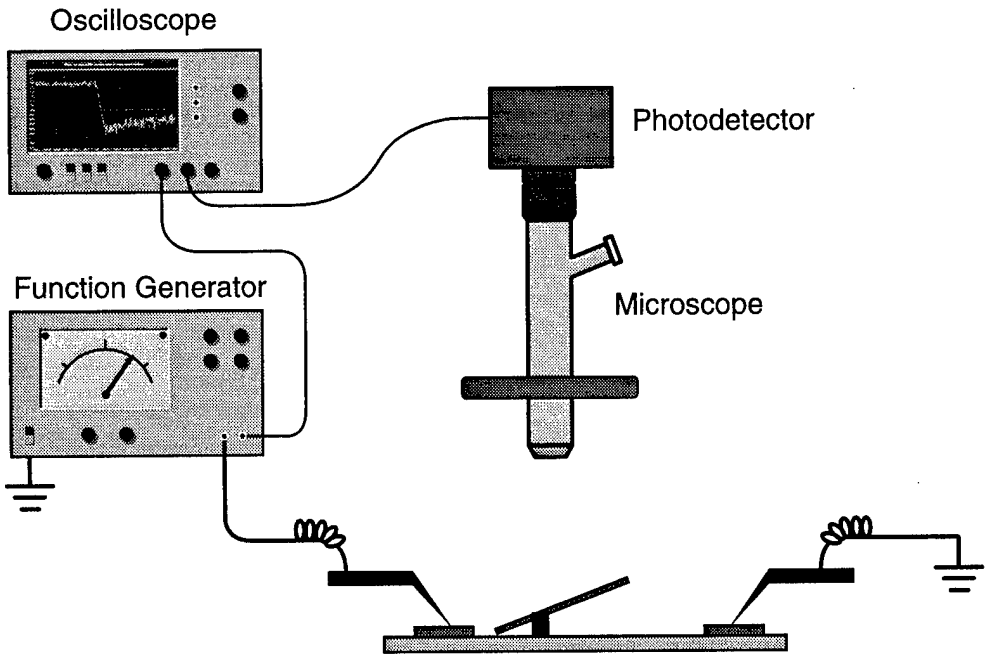

Figure 28. Speed measurement test setup.

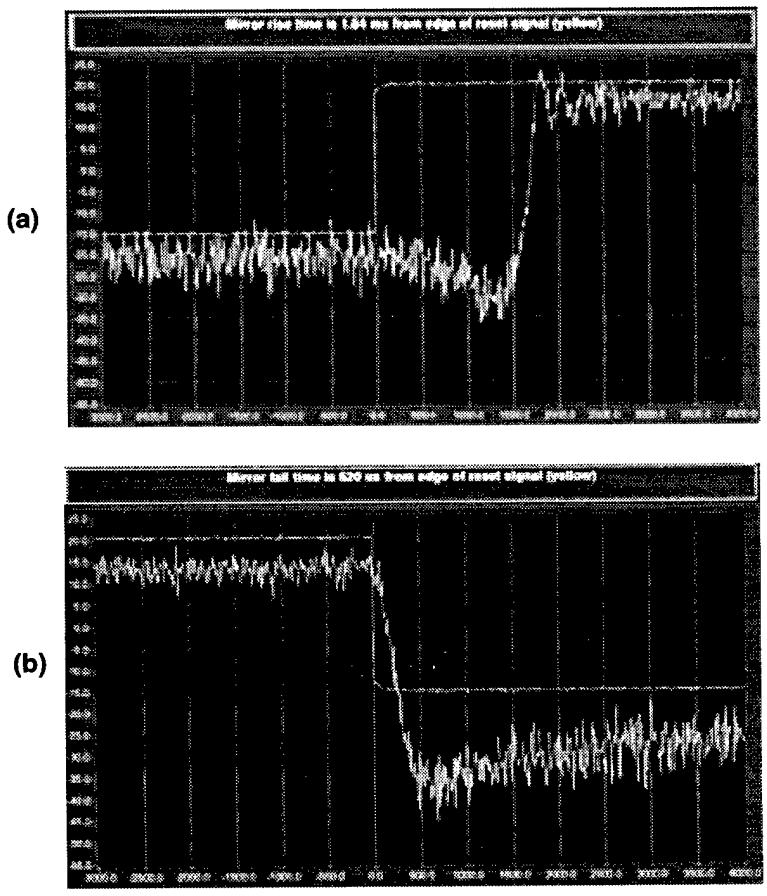

Figure 29. Speed measurement of the 350-μm long mirror (a) rise time and (b) fall time. The lag between trigger point and onset of the detected wave form is a result of the starting point of the beam leaving the aperture.

VII. CROSSBAR SWITCH DEVICE AND PACKAGE DESIGN AND FABRICATION

A. Overview

This chapter describes the design and fabrication of the device (chip) and package for a 4×4 crossbar switching demonstration. Section VII.A reviews the system design to summarize how the system drives device requirements. Section VII.C discusses the optical beam geometry at the chip, which determines the chip size and shape. The hybrid packaging concept is also briefly introduced. Section VII.D describes the shutter chip (switching device) design. Section VII.E details the package design, and SectionVII.F describes how all the package parts are fabricated and integrated into subassemblies. Finally, Section VII.G outlines the equipment and procedures that were developed to assemble, align, and fasten the package parts into position, resulting in a finished optomechanical assembly.

B. 4 × 4 Crossbar Switch System

The goal of this project was to demonstrate the benefits of using micromachining to integrate multiple switching elements in a crossbar system. A 4×4 crossbar was chosen for the demonstration.

Figure 4 is a schematic of the interconnections required to perform a 4×4 crossbar function using on/off (shutter) switching elements of the type developed under this program. Passive four-way splitters and combiners are required to fan out the optical input signals to the switching elements and fan in the switched optical signals to the four output channels. Sixteen switching elements are thus required to implement the network, and, therefore, at least 16 switch elements should be integrated onto the switching chip (additional redundant elements are desirable to improve packaged switch chip yield).

Insertion loss of such a system constructed of single-mode fiber components is at least 12 dB optical (6 dB each from the single splitter and combiner in the path of any one signal), plus any excess losses in the splitters (typically a few tenths of a dB), and excess losses in the switches. Excess loss in the switches can result from less than perfect optical coupling efficiency of the light leaving and entering the fibers and traversing lenses, etc., and from partial blockage of light in the switch on state. Crosstalk in the system results from unwanted signals being incompletely attenu-

ated by switches in their off state, caused by insufficient shutter closure or misalignment. Thus degradation in the extinction ratio of a switching element can manifest itself as increases in either insertion loss, crosstalk, or both, depending on the source of the degraded extinction.

These system considerations thus dictate the goals of the device and package optical design: (1) to provide at least 16 switching points in a miniaturized and integrated fashion; (2) to provide access to the switching elements on the chip without partially blocking the beams, in order to preserve the on state; (3) to maximize off state extinction; and (4) to maximize manufacturability and yield.

C. Optical Design

An optical beam geometry had to be selected first to drive the shutter chip design and dimensions. The system was designed for use with Corning SMF-28 single-mode optical fiber at the 1310 nm wavelength, for compatibility with existing test equipment. (The 1550 nm wavelength could have been chosen, but beam spread due to diffraction would have been slightly worse.) The numerical aperture (NA) of SMF-28 fiber is approximately 0.13 at this wavelength, implying a beam divergence half-angle of about 7.5 degrees out the end of the fiber. A 1:1 (*2f-2f*) relay imaging lens system was selected for the package. This choice has several advantages: (1) the 1:1 arrangement simultaneously optimizes spot size and depth of focus (beam divergence) at the device, and these quantities are the same as those from the fiber; (2) aspheric microlens arrays well-corrected for unity conjugate ratio operation with sufficient numbers of elements and appropriate focal lengths were available from a previous project; and (3) a 1:1 system has a longitudinal magnification of unity, making alignment intuitive since the focal spot moves axially at the same rate as the fiber-to-lens spacing.

Results from the pixel test structures presented in Section 6 indicated that the largest shutters, 350 μm long by 80 μm wide, could be operated to raise up at an angle of 13 to 14 degrees. The shutter tip can thus be expected to reach 75 to 80 μm above the surface of the switching chip. These data, together with the known beam divergence and a conservative estimate for vignetting due to clipping the edge of the approximately gaussian beam, were used to determine the allowable chip

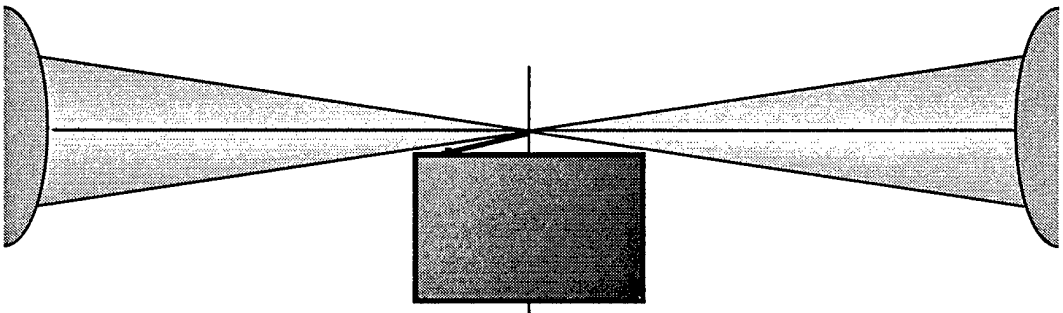

Figure 30. Schematic closeup of optical geometry at the chip.

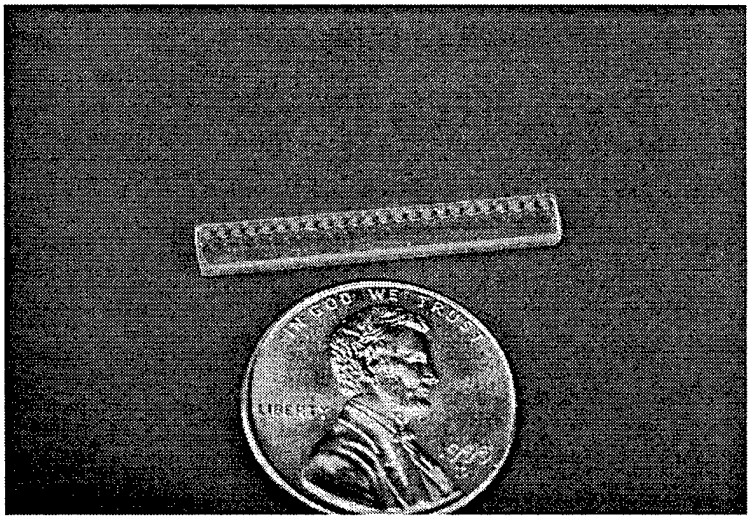

Figure 31. Photograph of 24 element aspheric refractive microlens array.

dimensions along the optical beam. A closeup of the chip and beam cross section as used in this calculation is shown in Figure 30. The edges of the optical beam shown in the figure indicate the $\pi\omega_0$ beam diameter, for which a circular aperture would pass ~99% of the light. Clipping by a straight chip edge will thus lead to an attenuation (excess insertion loss) of much less than 0.04 dB. A calculation using the known spacer thickness, tilt angle, and tip angle shows that the chip length should be a maximum of 1 mm, as drawn in the figure, to avoid clipping. Since the silicon substrate thickness is 625 μm, it can be seen that the aspect ratio of the chip cross-section is quite small, but this is unavoidable since it is required by the optics.

One of the refractive microlens arrays is shown in Figure 31. These lenses are approximately 950 μm in diameter, with a center-to-center spacing of 1016 μm. The lenses were made by Adaptive Optics Associates using a proprietary molding process. Twenty-four lenses in a linear

Figure 32. Shutter chip layout.

array are on each 1.8 mm thick glass substrate. The front and back focal lengths are both 1093 μm, leading to a chip-to-lens spacing of 2186 μm, as shown in Figure 30.

D. Shutter Chip Design

The optics design presented in Section VII.C and the microlens array spacing determined the overall chip dimensions. As just discussed, the "length" of the chip could be no more than 1 mm. Placing 16 switch elements on 1.016 mm centers requires that the chip be quite "wide" along the array. Adding a 17th switch element group and providing for bond pads and stepper alignment marks brought the chip width up to a full 20 mm stepper field width. The resulting layout is shown in Figure 32.

Because the lens center-to-center spacing is so large, four switch elements can fit side by side within each lens spacing. This was done to maximize redundancy and yield. The final layout has 69 total switch elements: 16 groups of 4 plus 1 group of 5, arranged so that one element is in the center of the chip. One bond pad drives each group of four or five elements, and a bond pad for the common "mirror" level connection is provided at both ends of the chip. The bond pads are in a three-layer staggered array to fit into the 1 mm chip height (length). Although the best-working double-hinge design and pixel designs were adopted from the test chip, nine variations were designed into the same stepper reticles because there was plenty of room in the *y* direction left in the 20 mm square stepper field. The shutter width was varied from 80 μm, proven to work in the test lot, to 90 and 110 μm, in order to relax lateral optical alignment sensitivity. A couple of landing tip and landing electrode geometry variations were also included to test hypotheses for potential improvements in operation or yield.

A layout of a single shutter element is shown in Figure 33. The address electrode that pulls the short (bottom) end of the element down comes in from the upper right. All other electrodes and the shutter (mirror) layer are electrically connected to avoid shorting and fusing or electrostatic

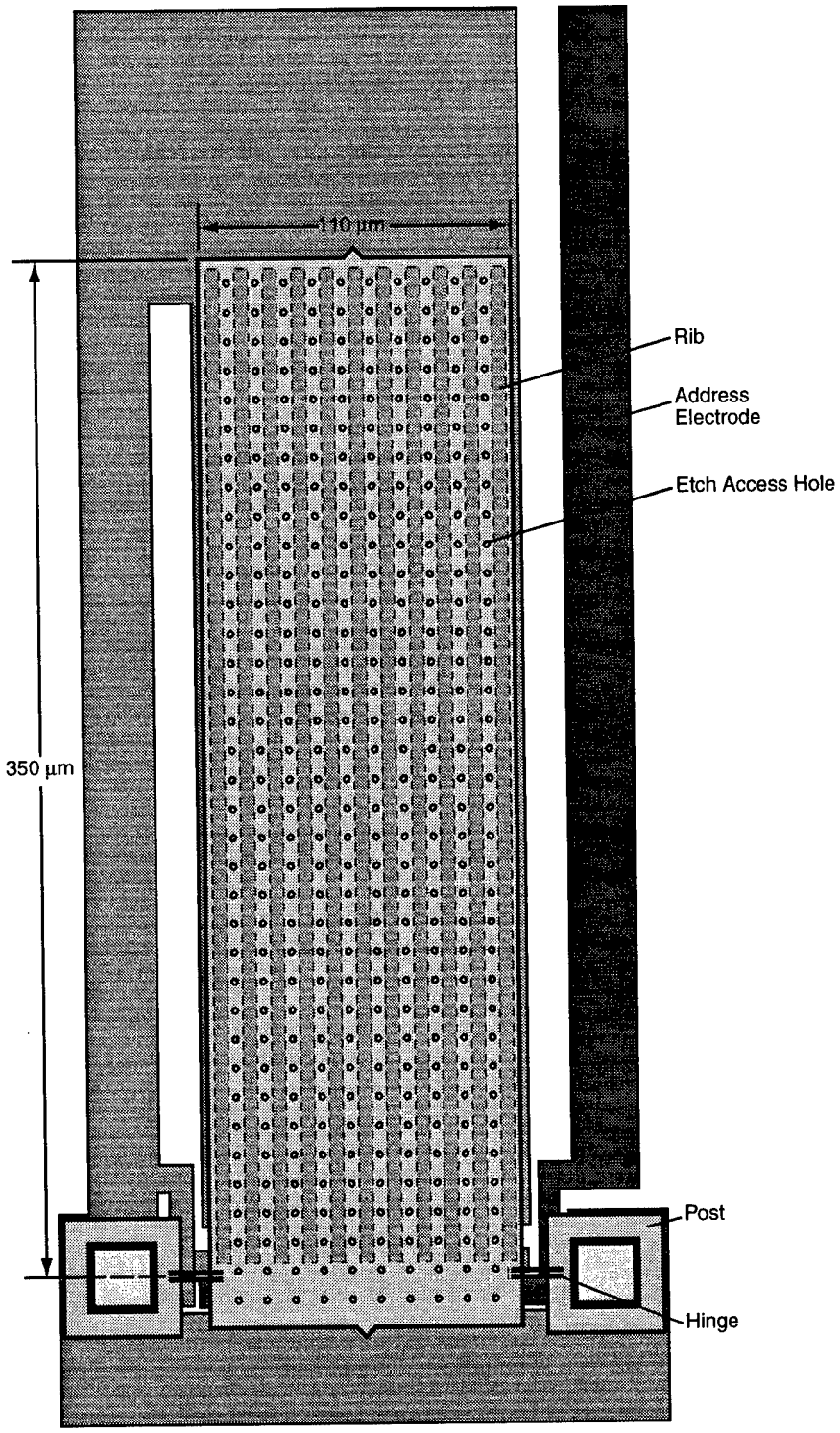

Figure 33. Layout of a single 350 (long-end length) by 110 mm wide shutter element.

disturbances during processing and operation. The stiffening corrugations (ribs) discussed earlier are visible, as are the etch access holes on 10 μm centers. Minor changes in the rib geometry (they no longer extend past the end of the shutter) were made to improve processing yield. A flat electrode area extends beyond the shutter tip to allow its use as a mirror for testing the shutters in a reflective test geometry.

The tip of the shutter's long end is designed to be centered approximately along the length (height) of the layout. To be exact, the tip was advanced 10 μm past the chip center line to take into account the shift back toward the center of the chip that occurs as the shutter tip is raised on a circular path centered on the hinges. This position of the shutter elements places them near the "bottom" edge of the layout in Figure 32. The top part of the layout is used for routing the signals from the bond pads to the address electrodes. The center lines of the shutters are marked on the top and bottom edges of the chips, and the elements are numbered (*e.g.*, 1A, 1B, 1C, 1D) to facilitate optical alignment. (A fully-functioning chip would require 16 shutters with the same letter, *e.g.*, C, to operate.)

We adapted the process described in Sections III and IV. Several changes in the new shutter chip resulted in challenges for the back-end process. First of all, the chip is 1×20 mm. an extreme aspect ratio that causes handling problems and nonuniform gas flow in the chamber. Second, the 80-μm wide structures require longer undercut time. Our solutions to these issues are: (1) prepackaging a subassembly before undercut; (2) breaking down the undercut into more cycles; and (3) adding chip rotations for each cycle. Prepackaging increases package size to make handling easier. Breaking the undercut process into more cycles allows better cooloff in the overall longer plasma process. Finer chip rotation improves flow uniformity conditions.

E. Shutter Chip Package Design

To enhance packaged device yield and to decouple the optical alignment from chip fabrication and testing, we decided to separate the electrical and optical parts of the package design into two parts. The shutter chip and all required electrical drive leads would be packaged in a pin grid array header, and the fibers and microlenses would be mounted in a removable "lid." This allows

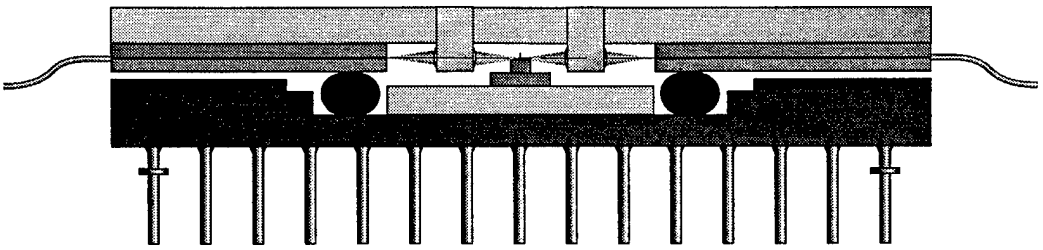

Figure 34. Side view cross-section of package concept. (Clamp not shown.)

the submicrometer-precision, single-mode fiber coupling to be done separately from chip mounting and testing. Once the fibers and lenses are fixed in place in the lid, the lid could be moved from header to header to test shutter chips. Only one or two complicated and critically aligned optical lids need be fabricated. Alignment of the lid to the chip can be done with lower precision (a few micrometers) positioners and fastening. Variations in die attach position and height can be accommodated by an adjustable clamp that holds the lid to the header. Spring return for the clamp to operate against is provided by sections of resilient O-ring material that are operated in a regime with little "memory." For the O-ring material, we chose a fluorocarbon elastomer that is resistant to "compression set" (memory) and is minimally chemically active (known not to degrade micromirror device reliability).

A side view of the assembled package concept is drawn to scale in Figure 34. The O-rings can be seen at their design compression of approximately 20%. The chip is raised up in the header on top of a pedestal, also made of silicon, and an alumina ceramic interposer. The interposer serves several functions: (1) it provides an intermediate lead frame for bond wires from the chip to the header, fanning out the closely spaced and staggered chip bond pads to the single-level, more widely spaced header bond pads; (2) it raises the chip to a height in the package appropriate to the commercially-available O-rings and position of the optical beam in the lid; (3) it helps in the alignment of lid to chip; and (4) it helps retain the O-rings in position. The O-rings are not complete; rather, they are just "logs" of extruded O-ring material that lie in the header as shown. Bond wires from the interposer to the header on the ends of the assembly not seen in the cross section prevent the O-rings from wrapping all the way around and providing a true sealing function.

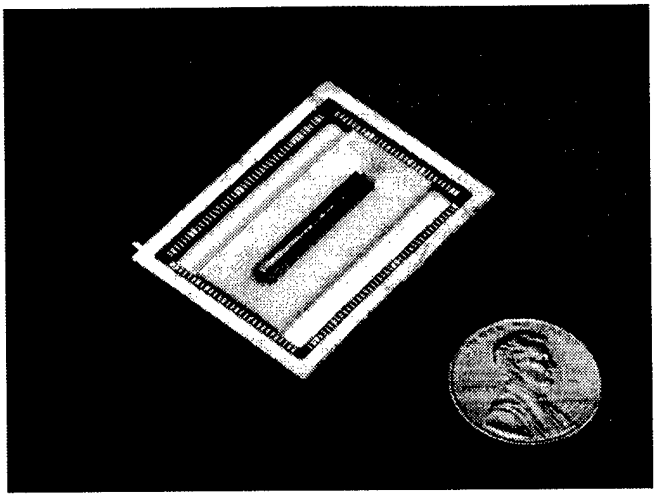

Figure 35. Photograph of header assembly.

Figure 35 is a photograph of the header/interposer/pedestal/chip assembly (referred to as the header assembly). The parts are all visible, except that the 1 mil (25 μm) gold bond wires connecting the chip to the interposer and the interposer to the header are difficult to see. The headers are 145 pin, 40 mm square, grid array ceramic packages that have been used on prior programs, so sockets were already available.

The optical fibers are held in custom silicon V-groove assemblies that hold both fiber arrays facing each other in a single unit with center-to-center spacing identical to that of the microlenses. Silicon V-grooves are made using orientation-dependent wet etching, a traditional silicon micromachining technique developed at Texas Instruments by Ken Bean and co-workers in the 1970s. These V-groove pieces are also laser-machined with a cutout to place the fiber ends accurately along the axis when the fibers are aligned flush with the edge of the cutout. Details of the V-groove chips are shown in Figure 36. The V-grooves themselves are designed to hold the center line of the fibers approximately 10 μm above the surface of the chip. Accurate registration of the fiber ends is ensured by clamping the accurately concentric glass fiber cladding between two such V-groove pieces as shown in the Figure 36(a) inset. The larger V-grooves toward the outer edges of the chip are designed to clear the 250 μm polymer primary coating on the fiber to be glued in place for mechanical strain relief. (Because of OH^- attack, fiber stripped to the bare glass cladding rapidly becomes brittle.) The actual V-groove chip mask layout is shown in Figure 36(b). Additional

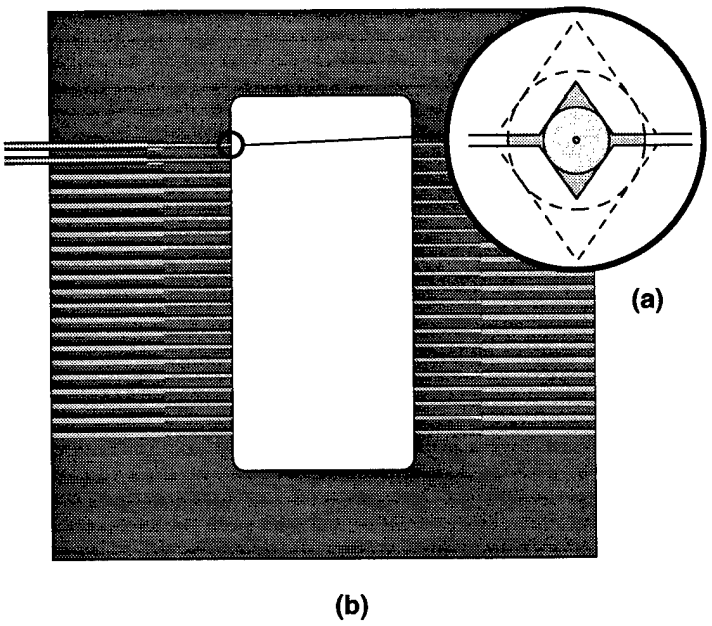

Figure 36 . V-groove silicon chip for holding optical fibers. (a) Pictorial drawing (inset shows end view of V-groove and fiber); (b) V-groove chip mask layout.

structures allow for optional sawing for polished (instead of cleaved) fiber ends, and glue channels and stops are provided for injecting glue and ensuring that it does not reach the optical fiber ends.

The lid is based on a fused silica (quartz) substrate, which holds the lenses and fibers. The transparency of the quartz allows the chip to be seen during alignment using visible light beams. The microlenses are held in precision laser-machined slots in the quartz lid. The V-groove assemblies are glued to the quartz lid, as well. Some details of the alignment procedure are given in Section VII.G. Photographs of a mockup (not optically aligned) of the lid assembly are shown in Figure 37.

F. Back-End Chip and Package Process Flow

The process flow required to produce the finished optical switch assemblies is shown in Figure 38. Parts coming into the process include the shutter chips after front-end processing; silicon pedestals simply sawed from silicon wafers or produced by the same process as the V-groove chips; custom thick-film gold on alumina interposer substrates; commercially obtained 145 pin ceramic headers; laser-machined quartz lids; microlens arrays; silicon wafers to be fabricated into V-groove chips; connectorized unbuffered optical fiber cables; machined clamps; and standard

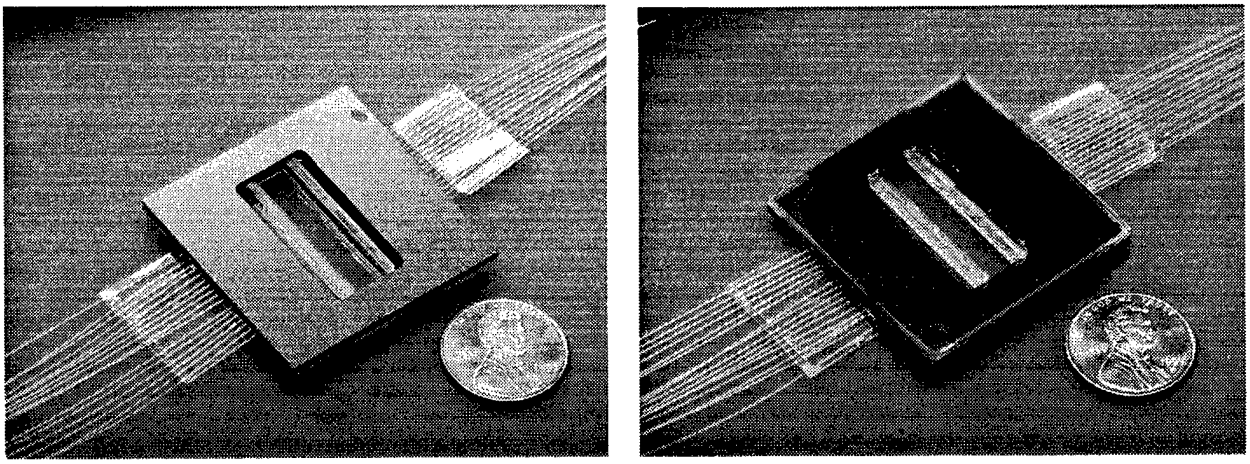

(a) (b)

Figure 37. Photographs of mock lid assembly. (a) Underside with microlens arrays; (b) top showing quartz substrate.

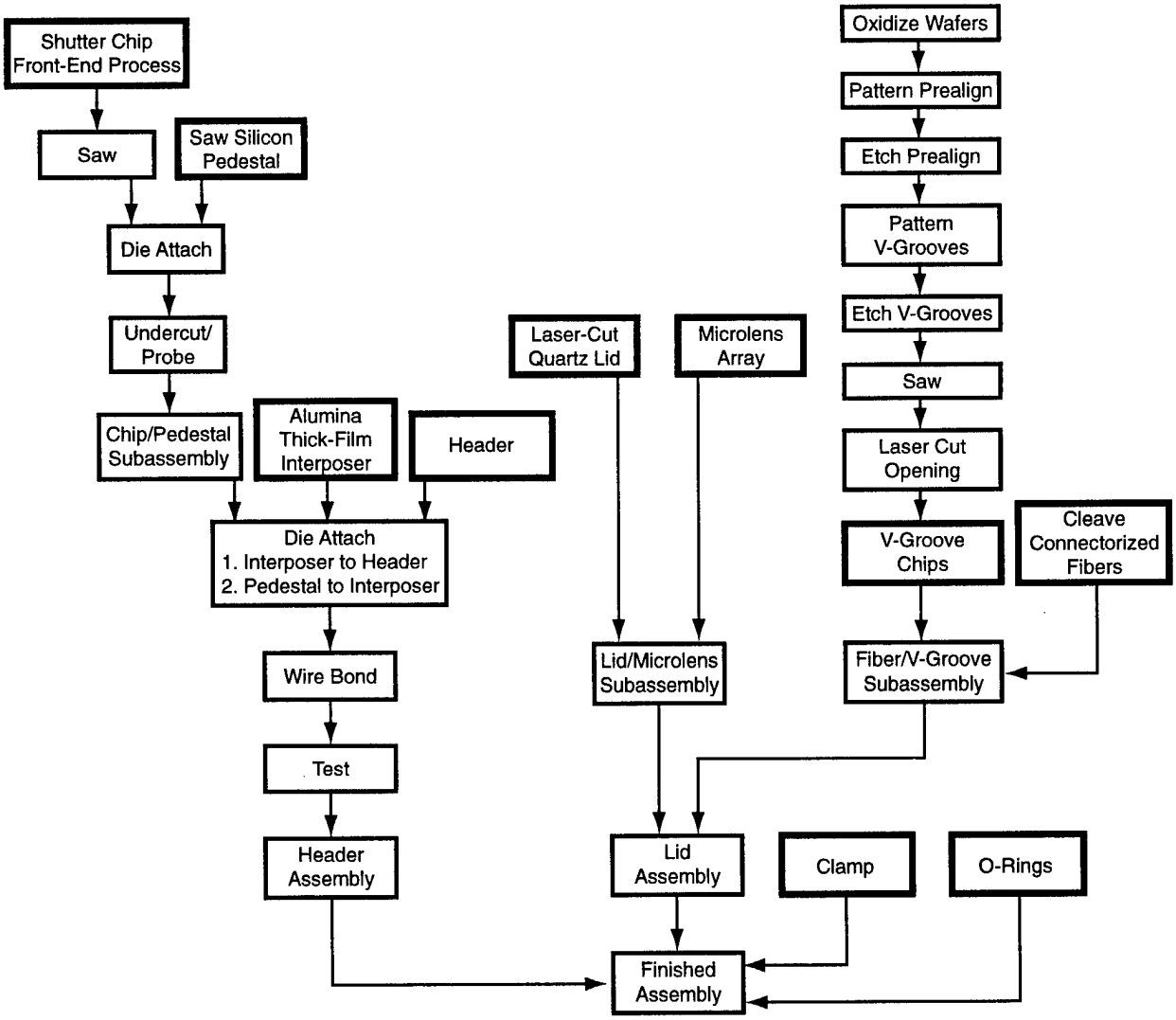

Figure 38. Back-end process flow chart.

extruded fluoropolymer O-ring stock. Custom fixtures, bonder programs, and other tooling were also constructed.

Header Assembly

Pedestals were made by sawing silicon wafers into 3×20 mm chips. Additional shallow saw cuts were made to guide chip placement on the pedestals.

We decided to perform the undercut process after the chips were die-attached to the pedestals. This permitted less handling of the chips after undercut, and the resulting assembly was more stable with respect to overturning than the nearly-square cross-section shutter chips themselves.

Custom alumina interposers were made by the Texas Instruments Defense Systems & Electronics thick-film shop. Both single-layer and multilayer (to allow for wider leads) substrates were made in the same run. Single-layer substrates were deemed adequate for the final assemblies.

Die attach of interposers to the headers and chip/pedestal subassemblies to the interposers were done using a die attach adhesive filled with 2 mil silver spheres to improve planarity of the chip surface. Both these joints were baked at the same time. Wire bonding was performed on a Kulicke & Soffa automatic bonder located in the Digital Micromirror Device production fab, using separate programs for the two ends of the chip. After wire bonding, the header assembly could be tested in a socket rather than the probe stations used at the chip level.

V-Groove Chips

V-groove chips were made on (100)-oriented 150 mm wafers using a two-step process. At both steps, the oxide hard mask is reactively ion etched, and then the silicon is etched using a wet potassium hydroxide orientation-dependent etch that stops on the (111) planes. The silicon etch rate is about 1 μm per minute, whereas the oxide mask etches at about 30 Å per minute.

Lithography for these noncritical and large (minimum 20 μm) geometries was performed on a contact mask aligner. The first lithography step is used to etch a prealignment "splay" pattern; it only takes 15 minutes to etch the 20 μm wide lines (14 μm deep). This pattern indicates the exact orientation of the crystal planes. For the second step, the mask is aligned to the prealign pattern, and the actual V-groove pattern is etched. After sawing the wafers into chips, the openings for the optical beams to cross are cut using CO_2 laser machining.

G. Optical Alignment, Assembly, and Test Procedure

Lid Assembly

Alignment and attachment of the fibers into the V-groove assembly is simplified by the design of the V-groove chips. The fibers are first cleaved, then carefully placed individually into the V-grooves. The two chips sandwich the fibers and are held using a spring clip. Once the fiber ends are aligned with the opening in the V-groove chip, glue is injected to fasten the assembly. Optical alignment of the microlenses to the fibers mounted in the V-groove chips is performed using separate commercial multi-axis positioners. The lenses are temporarily mounted to a "stick" for manipulation. After positioning and gluing using UV-curing adhesive, the "sticks" are broken off, leaving the lenses in place in the quartz lid. Finally the V-groove chip position is fine-tuned, and the fiber/V-groove assembly is likewise attached using UV-curing adhesive.

Final Assembly

A special six-axis alignment fixture was designed and built to position the lid with respect to the header and hold it in place while the clamps are fastened. An assembly drawing showing how this fixture goes together is shown in Figure 39.

The lid is held in a clamp designed to apply pressure directly over the O-rings. this clamp will in turn remain in place on the finished assembly. An additional actuator bar extends the clamp so that the 80-pitch knurled fine adjustment screws can act on this bar to shift, compress, and rotate the lid as required. A photograph of this fixture, which allows optical adjustment to be made while the shutters are being driven through a socket connection to the header, is shown in Figure 40.

After alignment, the socket-head screws that hold the clamp together and compress the O-rings are tightened, and the O-rings hold the lid in proper alignment. A photograph of a mockup of a finished assembly after removal from the alignment fixture is shown in Figure 41.

Optical Testing

The types of optical tests to be performed include extinction ratio, insertion loss, crosstalk, and actuation speed of individual devices as well as the complete optical crossbar system including splitters and combiners. These tests can all be performed in the alignment fixture, which provides electrical drive to the device.

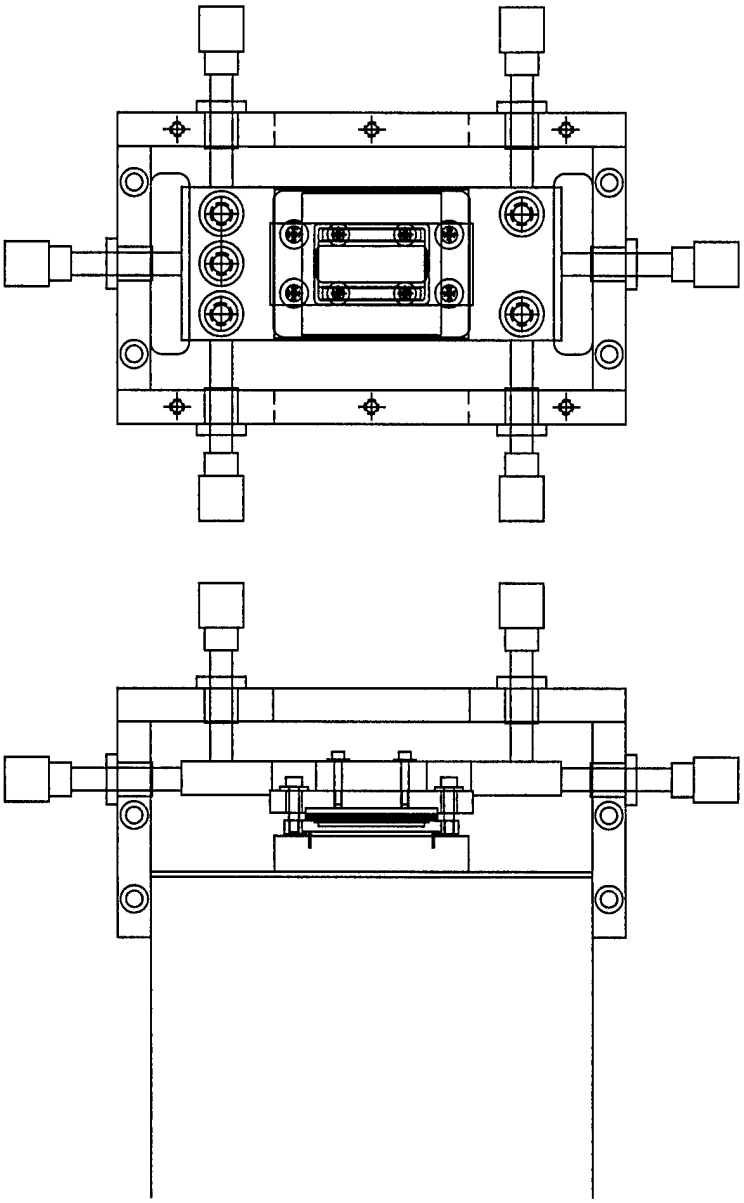

Figure 39. Assembly drawing of alignment fixture.

Single-mode fibers are used for connections to the device, and thus single-mode splitters are required. However, multimode combiners may be used to complete the crossbar network. A small improvement in overall insertion loss may result.

VIII. Future Work

The design and fabrication of the micromachined switching chip and optical package under this program have demonstrated the feasibility of fiber-optic switching using the asymmetric

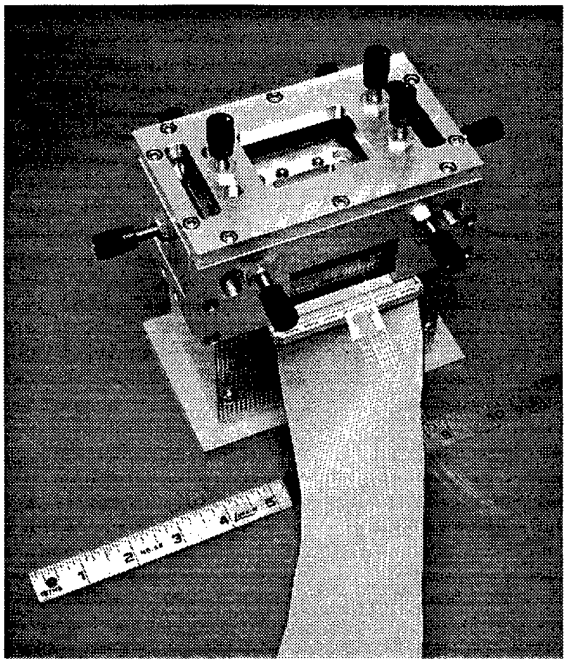

Figure 40. Photograph of alignment fixture with assembly in place.

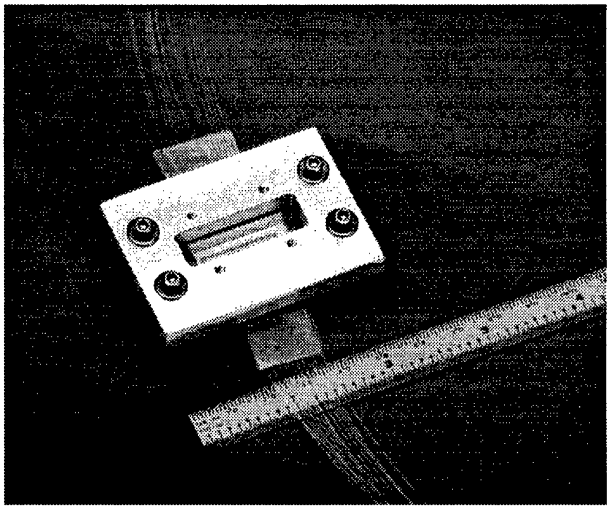

Figure 41. Photograph of finished optical assembly outside of alignment fixture.

micromirror shutter. Nevertheless, improvements are still possible to enable low-cost, high-volume manufacturing with higher performance.

Experience gained in processing the prototype shutter chips indicates that both design and process improvements are possible. The overall shape of the chip could be changed to simplify handling during chip processing and reduce steps in the packaging process. The shape and size of the shutter element itself, and details such as the spacing of etch access holes, are still open to further optimization for optical and mechanical performance as well as higher yield. Whenever a chip is redesigned, re-optimization and stabilization of the undercut process are also required. Stiction is still a concern, as it is in all MEMS devices, and passivation methods for these devices are under investigation.

As shown in the conceptual drawing of Figure 6, the ultimate version of the micromachined shutter device could incorporate micromachined fiber grooves and microlenses (or at least alignment structures for microlenses). Further development will be required to integrate the entire optical structure using micromachining techniques for "passive" self-alignment while achieving superior

and stable optical performance. Even in the prototype approach, which is a more hybrid assembly, automation could be applied to alignment and fastening to increase throughput in a manufactured version. Finally, the prototype had no provision for sealing the shutter device in a controlled atmosphere. A redesign would thus be indicated to enable the qualification of high-reliability devices to Bellcore standards for telecommunication applications.

The techniques we have developed on this program to stiffen large-area micromirror elements can and should be applied to new designs for $1 \times N$ switches (as opposed to on-off shutters) to be used as "active splitters and combiners" in implementing low-loss $N \times N$ switching networks[1]. These architectures avoid the high losses that result from the use of passive splitters and combiners together with on-off switches.

REFERENCES

1. R.A. Spanke, "Architectures for Large Nonblocking Optical Spade Switches," *IEEE J. Quantum Electron,* Vol. QE-22, pp. 964-967, 1986.
2. K. Padmanabhan and A.N. Netravali, "Dilated Networks for Photonic Switching," *IEEE Trans. Commun.,* Vol. COM-35, pp. 1357-1365, 1987.
3. L.J. Hornbeck, "Deformable-Mirror Spatial Light Modulators," Spatial Light Modulators and Applications III (Invited Critical Reviews), *Proc. SPIE* 1150, pp. 86-102, 1990.
4. R.M. Boysel, J.L. Leonard, G.A. Magel, T.G. McDonald, and G.C. Smith. "Integration of Deformable Mirror Devices With Optical Fibers and Waveguides," *Proc. SPIE* 1793, 1992.
5. T.G. McDonald, R.M. Boysel, and J.B. Sampsell. "Deformable Mirror Device-Based 4×4 Fiber-Optic Crossbar Switch," Conference on Optical Fiber Communication, 1990.
6. L.J. Hornbeck, "Digital Light Processing and MEMS: Timely Convergence of a Bright Future," presented at Plenary Session of Micromachining and Microfabrication, Austin, TX, October 1995.
7. S.P. Timoshenko and J.M. Gere, *Mechanics of Materials*, 1972.
8. S.P. Timoshenko and S. Woinowsky-Krieger, *Theory of Plates and Shells*, 2nd edition, 1959.